IEEE Photonics Journal
An IEEE Photonics Society Publication

Open Access

Efficient Brillouin Optomechanical Interaction Assisted by Piezomechanics on the SOI Platform

Volume 13, Number 3, June 2021

Ming Cheng
Kang Wang
Junqiang Sun

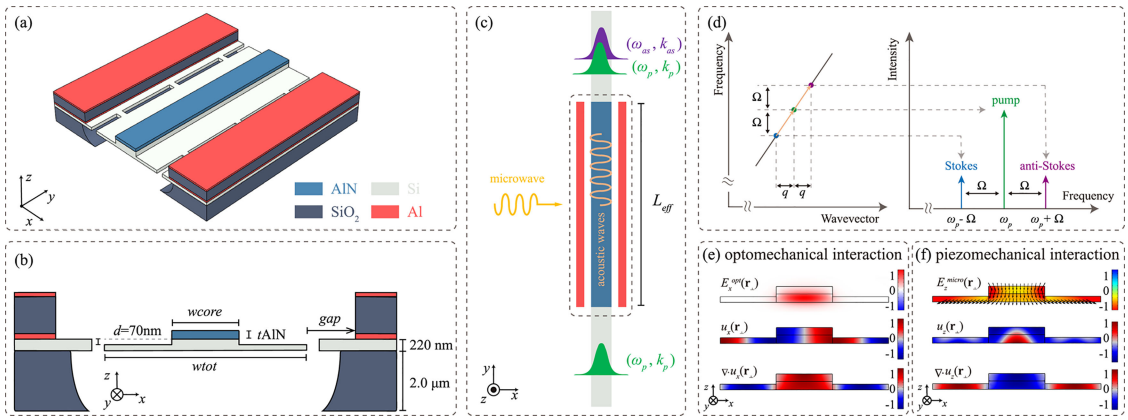

DOI: 10.1109/JPHOT.2021.3077732

Efficient Brillouin Optomechanical Interaction Assisted by Piezomechanics on the SOI Platform

Ming Cheng, Kang Wang, and Junqiang Sun

Wuhan National Laboratory for Optoelectronics, School of Optical and Electronic Information, Huazhong University of Science and Technology, Wuhan 430074, China

DOI:10.1109/JPHOT.2021.3077732

Manuscript received April 4, 2021; revised April 30, 2021; accepted May 3, 2021. Date of publication May 5, 2021; date of current version May 26, 2021. This work was supported by the National Natural Science Foundation of China (NSFC) under Grant 61875063. Corresponding author: Junqiang Sun (e-mail: jqsun@mail.hust.edu.cn).

Abstract: A hybrid silicon/aluminum nitride waveguide on the silicon-on-insulator platform is proposed to achieve an efficient Brillouin optomechanical interaction. Both intra-optical-mode and inter-optical-mode Brillouin scattering can be achieved. The novel arrangement of symmetric electrodes provides out-of-plane electric fields for piezoelectric materials and the possibility of suspended waveguides and cavities. The piezomechanical interaction coupling strength and the Brillouin optomechanical interaction coupling strength are numerically calculated. The simulation results show that near-unity internal conversion efficiency from the microwave domain to the optical domain can be achieved. Relatively low microwave power can be used to produced up to 5 order sidebands acousto-optical modulation. The proposed scheme paves the way for efficient classical and quantum application in integrated silicon photonics.

Index Terms: Optomechanics, photon-phonon interaction, Brillouin scattering, integrated silicon photonics.

1. Introduction

The interaction between a mechanical motion and an optical field has attracted considerable interest in classical [1]–[3] and quantum fields [4]–[8]. In the optical fiber community, the photon-phonon interaction is known as Brillouin scattering (BS). Recently, the development of nanofabrication has turned the attention of researchers to microscale and nanoscale structure. It was found that radiation pressure forces significantly enhance the photon-phonon interaction within high-index contrast materials [9]. In the integrated silicon photonics, van Laer *et al.* found that light and hypersound can be highly confined in a silicon photonic nanowire which can realize net on-chip Brillouin gain [10], [11]. Rakich group found that silicon ridge membrane can mediate both intramode forward stimulated Brillouin scattering (FSBS) [9] and stimulated intermode Brillouin scattering (SIMS) [12]. Large FSBS gain has been observed [13]. Brillouin intermode modulation [14], on-chip Brillouin laser [15], resonately enhanced Brillouin amplifier [16], microwave filter [17], [18], backscatter-immune injection-locked Brillouin laser [19] have been demonstrated based on SIMS. Nanoscale photon-phonon interaction (including optical wave-guiding Brillouin scattering and cavity optomechanics) is applied to trap and control dielectric particles [20], squeeze light [21], and quantum nondemolition (QND) detection of light intensity [22]. However, the Brillouin

optomechanical coupling is restricted by optical and mechanical dissipations, and the strength of the acoustic field driven by the injected light.

High-efficiency electromechanical devices have been achieved on the Aluminum Nitride (AlN) platform because of the sizable piezoelectric coefficient. AlN is not only an attractive electromechanical material but also an excellent optical waveguide material. Firstly, the operation wavelength ranges from the ultraviolet to infrared wavelengths owing to the large bandgap (6.2 eV). In contrast, the operation wavelength of silicon is restricted above 1100 nm, thus limiting the application of the ultraviolet and visible wavelengths. Secondly, AlN can handle tremendous optical power because of low linear loss and the absence of two-photon absorption as well as the free-carrier effects on telecom wavelengths(1530-1565 nm). Thirdly, the non-centrosymmetric crystal structure of AlN enables a linear electro-optical effect and an efficient wavelength conversion based on the second-order nonlinear effect. Finally, a superior thermal conductivity and a small thermo-optical coefficient make AlN devices more stable to temperature fluctuations. Electromechanical Brillouin scattering in under-etched aluminum nitride waveguides has been observed [23]. However, aluminum nitride waveguides are not compatible with the integrated silicon photonics which is complementary metal-oxide-semiconductor (CMOS) compatible. Besides, the small refractive index of AlN leads to weak Brillouin optomechanical coupling strength, and extra modal converters are required to build a bridge between the AlN waveguide and the silicon waveguide in integrated silicon photonics, owing to the refractive index difference between silicon and AlN.

Piezo-optomechanical interaction has attracted much interest recent years. Balram *et al.* found interfering phonons electromechanically and optomechanically generated [24]–[26]. Kittlaus *et al.* have looked at integrating aluminum nitride with silicon to avoid under etching the SOI stack [27]. Although this structure increases the robustness of the device, it is not efficient in microwave-to-optical conversion due to the acoustic field is confined in the silicon dioxide and the most of the microwave energy is dissipated.

This paper proposes a hybrid waveguide composed of a thin AlN film deposited on a silicon ridge waveguide and can benefit from both piezoelectric coupling of the AlN and a huge optomechanical coupling strength of silicon. The symmetric out-of-plane electric field is provided by a novel electrode arrangement to convert the microwave to a mechanical motion within the AlN, and the optomechanical interaction occurs in the silicon ridge waveguide where optical fields are confined. The features of the piezomechanical and the optomechanical interactions are studied using Hamiltonian description. The coupling strength and the conversion efficiency from the microwave to optical waves are calculated using the parameters of realistic physical structures. The trade-off between the piezomechanical and the optomechanical interactions gives rise to an optimal value of the hybrid waveguide structure, resulting in a near-unity internal conversion efficiency. High order optical phase modulation can be achieved with relatively low microwave power. The phase-matching condition of inter-optical-mode interaction enable integrated non-reciprocal devices. The proposed hybrid waveguide provides an platform to achieve efficient piezo-optomechanical transduction between microwave and optical frequency.

2. Intra-Optical-Mode Interaction

2.1 Piezo-Optomechanical Coupling Strength

Fig. 1(a) shows the isometric view of the suspended hybrid waveguide, which can simultaneously confine both optical and mechanical modes. The device in our scheme are designed on the commercial silicon-on-insulator (SOI) wafer with a 220-nm crystalline silicon layer above an oxide layer of thickness 2 μm. Fig. 1(b) shows the cross-section of the device. The hybrid waveguide has a ridge structure, which has several advantages: (i) because the optical mode is concentrated in the waveguide's core region, the device has a higher tolerance for the manufacturing process and a lower transmission loss induced by the roughness, enabling low pumping threshold, efficient power consumption, and a high Q-factor for an optical cavity; (ii) the properties of the trapped optical and mechanical modes, such as the effective refractive index of the optical modes and the

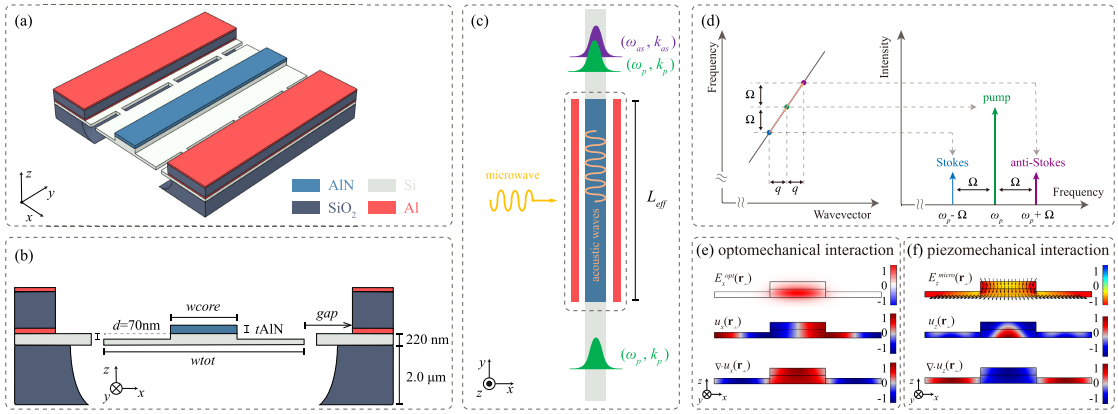

Fig. 1. The schematic illustration of the proposed device and intra-optical-mode interaction. (a) Artistic representation of the proposed device; (b) The cross-section of the suspended hybrid waveguide and the electrode configuration (c) depicts the optical and acoustic modes profile. (d) sketches the phase-matching diagram of intra-optical-mode process and optical spectrum of pump light and sidebands. (e) plots the symmetric distributed x-direction electric field $E_x^{opt}(\mathbf{r}_\perp)$ profile of the fundamental optical mode and the asymmetric distributed x-displacement $u_x(\mathbf{r}_\perp)$ and the symmetric distributed x-strain $\nabla{\cdot}u_x(\mathbf{r}_\perp)$ profiles of the excited S_0 lamb-like mechanical mode. Note that both $E_x^{opt}(\mathbf{r}_\perp)$ and $\nabla{\cdot}u_x(\mathbf{r}_\perp)$ are symmetric with respect to the center of the hybrid waveguide, which mediate efficient optomechanical interaction. (f) plots the x-symmetric distributed z-direction electric field $E_z^{micro}(\mathbf{r}_\perp)$ profile on the microwave mode and z-displacement $u_z(\mathbf{r}_\perp)$ and z-strain $\nabla{\cdot}u_z(\mathbf{r}_\perp)$ profiles of the excited S_0 lamb-like mechanical mode. The arrows indicate the direction of the microwave electric fields. The overlap integral of $E_z^{micro}(\mathbf{r}_\perp)$ and $\nabla{\cdot}u_z(\mathbf{r}_\perp)$ determines the piezomechanical coupling strength.

frequency of the mechanical modes, can be individually tuned by varying the width of the core ($wcore$) and the total width of slab ($wtot$), respectively. The ridge of the waveguide is defined by 70-nm-deep etches ($d = 70$nm). This is the typical value for grating couplers in integrated silicon photonics. The deposited AlN layer has the same width as the slab width. The thickness of AlN (tAlN) needs to be carefully designed. On the one hand, the thicker AlN corresponds to a larger overlap integral between the electric field of the microwave and the strain field of the mechanical mode, leading to a higher conversion efficient from the microwave to the mechanical wave. On the other hand, hybrid waveguides with thinner AlN layers can mediate more efficient optomechanical interactions, since the optical field is mainly confined in the silicon. In addition, the thickness of the AlN layer should not be too large to prevent from the higher-order Lamb waves. The design of the electrode configuration is a key point in this device. On the one hand, the electrode cannot be in contact with AlN, otherwise it will produce a large metal-induced optical loss, on the other hand, SiO_2 cannot be deposited between the electrode and AlN for reducing the metal-induced optical loss, because the acoustic field will leak from the hybrid waveguide into the SiO_2, thus reducing the efficiency of the acousto-optical interaction. In our electrode configuration, two pairs of coplanar electrodes are located at each side of the hybrid waveguide. Each pair of the coplanar electrodes consists of two electrodes (above and below) and a SiO_2 layer sandwiched between them. The upper electrode is the signal pad, and the lower electrode is the ground pad. The gap between the waveguide and the electrodes (gap) should be large enough to avoid metal-induced optical and mechanical losses. The strongest electric field distributes between the upper and lower electrodes, whereas the electric field in the AlN is much weaker. Our electrode configuration is completely different from the traveling-wave electrodes in modulators or detectors where the SiO_2 layer is sandwiched between the electrodes and the waveguide (thus it is tough to make the waveguide suspended). We re-emphasize that this electrode arrangement can provide a symmetrical out-of-plane electric field to the AlN without an additional SiO_2 layer sandwiched between the electrodes and the waveguide, thereby matching the symmetrical electrostrictive force and the radiation pressure within the suspended optical waveguide. The oxide layer beneath the top

silicon layer is removed by wet-etching to suspend the hybrid waveguide. The fabrication is potential since similar devices have been fabricated by the process [28], [29]. We use a commercial finite element software COMSOL to simulate the piezoelectric effect and to solve the supported optical field modes of the hybrid waveguide. In this study, we theorically investigate the piezomechanical and both of intra-optical-mode and inter-optical-mode Brillouin optomechanical conversions with varying structural parameters.

Fig. 1(c) shows the principle of the intra-optical-mode piezo-optomechanical interaction. The microwave (ω_m, K(ω)) is piezoelectrically coupled to the mechanical mode (Ω, $q(\Omega)$) in the hybird waveguide through the deposited AlN. On the other hand, the pump light (ω_p, $k(\omega_p)$) is coupled to the acoustic wave through photoelastic and moving bounding effect, and scattered to optical sidebands ($\omega_p \pm \Omega$, $k(\omega_p \pm \Omega)$) in the same optical mode. Both piezo-mechanical and optomechanical process require the phase-matching and frequency-matching condition. For piezo-mechanical transduction, frequency-matching requires $\omega_m = \Omega$ and because the microwave is normal incident to the light propagating axis, thus the axial wavevector should be $K = q = 0$. Fig. 1(d) shows the condition of phase-matching and frequency-matching in optomechanical process. The optical sidebands require $k(\omega_p \pm \Omega) = k(\omega_p) \pm q$. Since $q = 0$, the intra-optical-mode scattering process is not perfectly phase-matched with mismatching $|\triangle q| = |k(\omega_p \pm \Omega) - k(\omega_p)| \approx \Omega / v_g < 125 \mathrm{m}^{-1}$, where $v_g = \partial\omega/\partial k \sim 8 \times 10^7 \mathrm{m/s}$ is the group velocity of the guided optical mode. Note that we assume the dispersion is linear over frequency detuning of ~GHz range, which is well-satisfied in the hybrid waveguide. The electric field, optical field and the acoustic mode are sinusoidally vibrated along the propagation direction when a phase mismatching existing. However, as long as $|\triangle q L_{\mathrm{eff}}| \ll 1$ is satisfied, the process is approximately phase-matched. In the simulation, $L_{\mathrm{eff}} = 400 \mu m$ and $|\triangle q L_{\mathrm{eff}}| \approx 0.05 \ll 1$.

In addition, the microwave, acoustic and optical fields need to have the same symmetry. For Brillouin optomechanical interaction, the strength of the optomechanical coupling g_{om} is proportional to the overlapping integration of the x-electric fields $E_x^{opt}(\mathbf{r}_\perp)$ of the pump and the scattered light, and the x-strain field of the acoustic field $\nabla \cdot u_x(\mathbf{r}_\perp)$. Fig. 1(e) plots the distribution of the optical and acoustic fields in intramode optomechanical process. Since both of the pump light and the scattered light are fundamental modes, which are symmetric to xy-plane, the strain field symmetrically distributed in the xy-plane can mediate efficient optomechanical process. For piezomechanical process, the strength of the piezomechanical coupling g_{pm} is proportional to the overlapping integration of the z-electric field of the microwave $E_z^{micro}(\mathbf{r}_\perp)$ and z-strain field of the acoustic field $\nabla \cdot u_z(\mathbf{r}_\perp)$. Fig. 1(f) plots the distribution of the microwave field and mechanical vibration in piezomechanical process. Besides, $E_z^{micro}(\mathbf{r}_\perp)$ should also be symmetric to xy-plane to efficiently produce the symmetric mechanical vibration.

Piezomechanical interaction coupling strength g_{pm} is used to describe the efficiency of converting the microwave to a mechanical motion. The mechanical resonance of a hybrid waveguide is caused by the piezomechanical motion in a sputtered polycrystalline AlN film that has similar properties as a single crystalline AlN with a c-axis out-of-plane orientation. The out-of-plane electric field is applied to match the orientation and excite the piezomechanical mode. Figs. 2(a) and (b) show the piezomechanical interaction coupling strength g_{pm} as a function of $wcore$ and tAlN with different gap, respectively. It can be observed that as $wcore$ increases, g_{pm} decreases because the overlap of the out-of-plane field and the z-direction strain field in the AlN film decreases. When tAlN is increased from 50 to 300 nm, g_{pm} increases because of a larger overlap between the out-of-plane electric field and the z-direction strain field in the AlN film as well. g_{pm} reduces with the increase of gap owing to the decaying out-of-plane electric field away from the electrode. The peak in the curve is due to the fact that near the mode hybridization point, the modal distribution of the driven acoustic mode is slightly different from the eigenmode distribution, resulting in a peak point that does not satisfy the trend of the curve.

The Brillouin optomechanical interaction coupling strength g_{om} is related to the Brillouin gain coefficient which describes the efficiency of the energy transfer from the pump wave to the Stokes and anti-Stokes waves. The variations of the Brillouin optomechanical interaction coupling strength with the different structure parameters of the hybrid waveguide are shown in Figs. 2(c)–(h). We assume

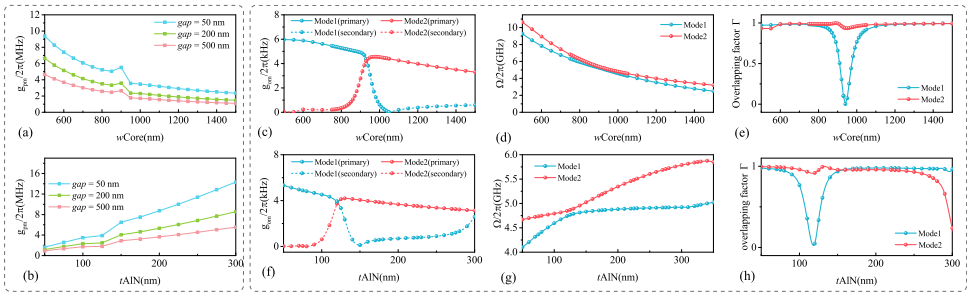

Fig. 2. The piezomechanical interaction coupling strength versus (a) the width of the waveguide core $wcore$ and (b) the AlN thickness tAlN with $gap = 50, 200, 500$nm, respectively. (c), (d) and (e) show the Brillouin optomechanical coupling strength, eigenfrequency of the mechanical mode which can mediate the strongest optomechanical interaction and the overlapping integral factor of the driven mechanical vibration with different $wcore$, respectively. (f), (g) and (h) show the Brillouin optomechanical coupling strength, eigenfrequency of the mechanical mode which can mediate the strongest optomechanical interaction and the overlapping integral factor of the driven mechanical vibration with different tAlN, respectively.

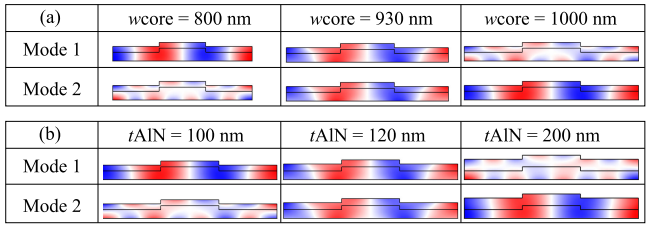

Fig. 3. (a) x-direction displacement of the driven mechanical vibration mode 1 and mode 2 with $wcore$ of 800 nm, 930 nm and 1000 nm, (b) x-direction displacement of the driven mechanical vibration mode 1 and mode 2 with tAlN of 100 nm, 120 nm and 200 nm.

that the length of the optomechanical waveguide is $L_{\text{eff}} = 400\mu m$. The Brillouin optomechanical coupling strength does not change with *gap* because the Brillouin optomechanical coupling mainly occurs within the waveguide's core region where the optical field is confined. Figs. 2(c) and (f) show the Brillouin optomechanical interaction coupling strength as a function of $wcore$ and tAlN, respectively. Two mechanical vibration modes can be driven by the optical force distribution within the hybrid waveguide. The solid and the dash lines indicate the primary and secondary mechanical modes under different structural parameters, respectively. The transition points by the mechanical vibration mode hybridization can be observed in both figures. Figs. 2(d) and (g) show the frequency of the two mechanical modes vary with different $wcore$ and tAlN. As $wcore$ and tAlN increase, the two dispersion lines get closer at the transition point and then seperate from each other. We also calculate the surface overlapping factor Γ between the driven mechanical vibration mode and the eigen mechanical mode. $\Gamma = (\int \mathbf{u}_1 \cdot \mathbf{u}_2^* d\mathbf{r})^2 / ((\int |\mathbf{u}_1| d\mathbf{r}) \cdot (\int |\mathbf{u}_2| d\mathbf{r}))$. Here, $\mathbf{u}_1$ is the driven mechanical vibration, which is coupled to the microwave mode, composing of a serial of eigen mechanical modes. And, $\mathbf{u}_2$ is the eigen mechanical mode that can mediate the strongest optomechanical interaction with the optical fundamental TE mode. The overlapping factor is splitted around the transition point due to the evolution of y-direction displacement of the driven mechanical vibration, indicating that the driven mechanical vibration has a complicated characteristic.

2.2 Mode Hybridzation

To illustrate the effect of mode hybridization on the Brillouin optomechanical interaction coupling strength, the modal evolution of the two hybrid mechanical vibration modes is presented. Fig. 3 shows the x-direction displacement field of the mechanical vibration modes with $wcore$ of 800 nm,

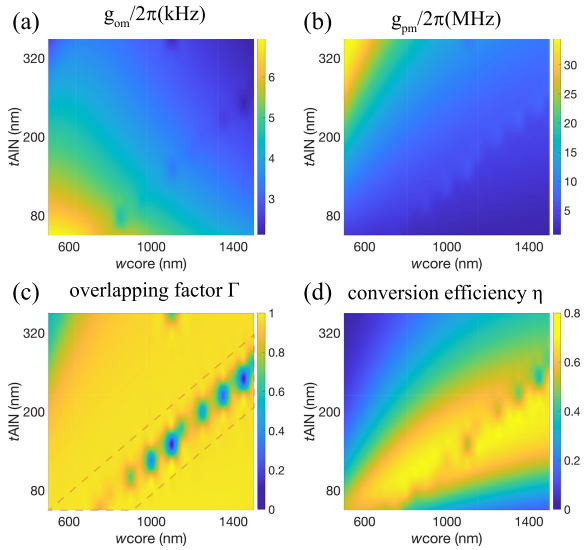

Fig. 4. (a) The Brillouin optomechanical coupling strength, (b) the piezomechanical coupling strength, (c) the overlapping factor and (d) the conversion efficiency versus $wcore$ and tAlN, respectively.

930 nm and 1000 nm. It can be observed from Fig. 3(a) that when $wcore$ is 800 nm, the difference in the frequencies between the two mechanical vibration modes is large enough to avoid mode hybridization. The x-displacement of mechanical vibration mode 1 matches the optical force distribution of the TE optical mode, leading to an efficient Brillouin optomechanical interaction while the mechanical vibration mode 2 mismatches. When $wcore$ is approximately 930 nm, the modal distribution and the eigenfrequencies of the two mechanical vibration modes cannot be distinguished from the each other. Both mechanical vibration mode 1 and 2 are simultaneously driven with the input microwave signal, and two pairs of Stokes and anti-Stokes optical waves with a slight frequency difference will be excited. When $wcore$ further increases to 1000 nm, the eigenfrequencies and the modal distribution of the two mechanical vibration modes are separated from each other again. Moreover, the mode 2 becomes the primary mode in the Brillouin optomechanical interaction.

2.3 Conversion Efficiency η

Thus far, we investigate the changes of the piezomechanical and the Brillouin optomechanical strength coefficients with different structural parameters. We now seek the optimum size of the waveguide to deliver a maximum coupling efficiency. Figs. 4(a) and (b) show the variations of the Brillouin optomechanical interaction coupling strength and the piezomechanical interaction coupling strength with $wcore$ and tAlN. The largest coupling strength of the Brillouin optomechanical interaction g_{om} and the piezomechanical interaction g_{pm} is located at the left-bottom corner (i.e., with small $wcore$ and small tAlN) and left-top corner (i.e., with small $wcore$ and large tAlN) respectively. We neglect the external loss of the microwave and the optical fields and use Eq. (9) to obtain the internal coupling efficiency from the microwave domain to the optical domain. A normal mechanical field Q-factor $Q_b = 2 \times 10^3$ and intrinsic Q-factor of microwave field $Q_a = 2 \times 10^3$ are assumed. The corresponding amplitude decay rates of the mechanical and microwave fields are $\kappa_b/2\pi = 2.5$MHz and $\kappa_{a,0}/2\pi = 2.5$MHz with $\Omega/2\pi = 10$GHz. Figs. 4(c) and (d) show the mechanical overlapping factor and the conversion efficiency versus the structural parameters. The discontinuity observed in both of the figures is caused by the mode hybridization. The largest coupling efficiency of 0.8 can be achieved under certain combinations of the structural parameters due to the collective effect of the piezomechanical and Brillouin optomechanical interactions.

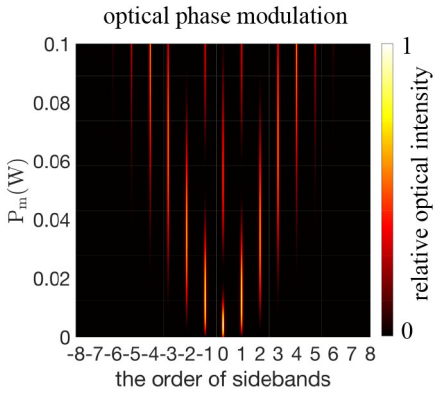

Fig. 5. Intramode optical phase modulation. Up to 5-order sidebands can be produced with $P_\mu = 0.1$ W.

2.4 Intramode Optical Phase Modulation

For intramode optomechanical process, the pump light is scattered into Stokes and anti-Stokes light with the same strength. The process is a typical acousto-optic modulation and the relative optical intensity of the sidebands is given by the Bessel functions. The injected microwave energy is piezoelectrically coupled into mechanical vibration, the strength of which determines the depth of optical phase modulation. Figs. 5 shows the relative optical intensity of sidebands versus the power of injected microwave P_μ. Up to 5-order sidebands can be produced with $P_\mu = 0.1$ W.

3. Inter-Optical-Mode Interaction

The case of inter-optical-mode interaction is more complicated, so here we make a brief introduction to throw light on it. Figs. 6(a) depicts the cross-section of the hybrid waveguide used to achieve inter-optical-mode interaction. For inter-optical-mode interaction, the pump is incident in the fundamental mode and scattered to the first order modes. To mediate efficient Brillouin optomechanical interaction, the strain fields of the driven mechanical vibration in the x-direction should be antisymmetric, which means the displacement field in the x-direction is symmetrically distributed. According to the standing-wave condition, the width of the slab needs to be an even multiple of the waveguide core. Considering that a wider waveguide slab w_{tot} will lead to a lower electric field strength in the AlN as well as reduce the stability of the suspended structure, the slab of the ridge waveguide is designed as twice the width of the core region ($w_{tot} = wcore * 2$). Figs. 6(b) shows the x-direction electric fields of the fundamental optical mode field $E_{x,p}^{opt}(\mathbf{r}_\perp)$ and first-order optical mode field $E_{x,s}^{opt}(\mathbf{r}_\perp)$, as well as the displacement field $u_x(\mathbf{r}_\perp)$ and strain field $\nabla{\cdot}u_x(\mathbf{r}_\perp)$ of the eigen mechanical mode in the hybrid waveguide. Figs. 6(c) gives the distribution of the electric field $E_z^{micro}(\mathbf{r}_\perp)$ and the electric potential distribution in the z-direction, as well as the displacement field $u_z(\mathbf{r}_\perp)$ and strain field $\nabla{\cdot}u_z(\mathbf{r}_\perp)$ of the driven mechanical vibration. Unlike intra-optical-mode interaction, in order to driven this antisymmetric strain field, the phase difference between the two pairs of the microwave signal needs to be π. It can be seen that although the displacement field of the driven mechanical vibration is not the same as the x-direction displacement field of the eigen mechanical mode, a similar x-direction strain field can be excited by the microwave signal. Figs. 6(d) and (e) gives the phase-matching condition in the backward and forward cases, respectively. Since the frequency detuning between pump light ω_p and scattered light ω_s is the acoustic field frequency $\Omega(\sim \text{GHz}) = \omega_s - \omega_p$, for the hybrid waveguide, the wave vector of the fundamental optical mode is larger than the firsr-order. If the pump light is incident in the fundamental mode, the driven mechanical vibration needs to counterpropogate in the backward direction ($q_b = k_{p,b} - k_{s,b} < 0$) and satisfy the energy conservation ($\omega_{s,b} = \omega_{p,b} + \Omega$). When the pump light is incident in the first-order mode, the driven mechanical vibration needs

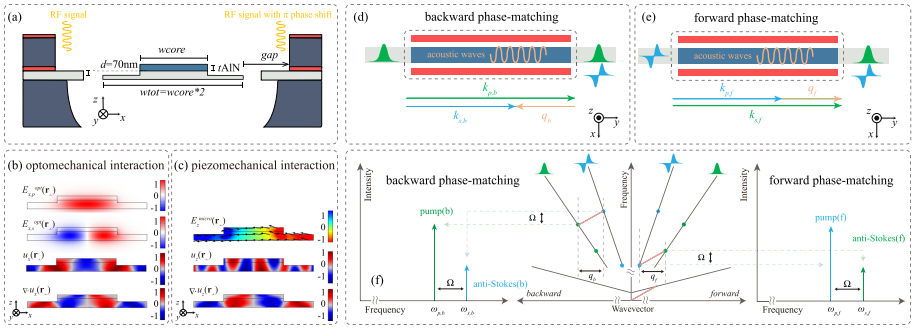

Fig. 6. The schematic illustration of the proposed device and inter-optical-mode interaction. (a) The cross-section of the suspended hybrid waveguide and the electrode configuration, there is a π phase shift between the two pairs of electrode; (b) plots the symmetric distributed x-direction electric field $E_{x,p}^{opt}(\mathbf{r}_\perp)$ and asymmetric distributed x-direction electric field $E_{x,s}^{opt}(\mathbf{r}_\perp)$ profile of the fundamental optical mode and the symmetric distributed x-displacement $u_x(\mathbf{r}_\perp)$ and the asymmetric distributed x-strain $\nabla{\cdot}u_x(\mathbf{r}_\perp)$ profiles of the excited S_0 lamb-like mechanical mode. Note that $\nabla{\cdot}u_x(\mathbf{r}_\perp)$ is symmetric with respect to the center of the hybrid waveguide. (c) plots the distributed z-direction electric field $E_z^{micro}(\mathbf{r}_\perp)$ profile on the microwave mode and z-displacement $u_z(\mathbf{r}_\perp)$ and z-strain $\nabla{\cdot}u_z(\mathbf{r}_\perp)$ profiles of the excited S_0 lamb-like mechanical mode. The arrows indicate the direction of the microwave electric fields. The π phase shift between the two pairs of electrode enable symmetric distributed x-displacement $u_x(\mathbf{r}_\perp)$, leading to efficient optomechanical interaction. (d) sketches the backward phase-matching diagram of inter-optical-mode process, in which the mechanical vibration counter-propogates with the optical waves. (e) sketches the forward phase-matching diagram of inter-optical-mode process, in which the mechanical vibration co-propogates with the optical waves. (f) sketches the backward and forward phase-matching diagram of inter-optical-mode process and optical spectrum of pump light and sidebands.

to copropogate in the forward direction ($q_f = k_{p,f} - k_{s,f} > 0$) and satisfy the energy conservation ($\omega_{s,f} = \omega_{p,f} + \Omega$). The energy conservation and phase matching conditions for the two cases are given in Figs. 6(f). When the energy conservation of inter-optical-mode interaction is satisfied, unlike intra-optical-mode interaction, only the anti-Stokes sideband can be phasing-matched. This single sideband modulation characteristic can improve the pump light conversion efficiency. The wavevector of the driven mechanical vibration can be controlled by making the electrodes as a periodical structure similar to interdigital transducer(IDT). The unidirectional transmission property can be used to realize on-chip integrated non-reciprocal devices.

4. Conclusion

We propose a hybrid ridge waveguide structure with a novel electrode arrangement that can be fabricated to achieve both intramode and intermode Brillouin optomechanical interaction. The deposited polycrystalline AlN provides an efficient piezoelectric conversion from the microwave domain to the mechanical field, and the large refractive index of the silicon enables Brillouin optomechanical interaction. We investigate the coefficients of the piezomechanics and Brillouin optomechanics with various structural parameters. The mode hybridization indicates that the microwave frequency should be adjusted according to the primary mechanical mode that matches the optical forces distribution. Considering the trade-off between the piezomechanical and optomechanical interactions,a near-unity internal coupling efficiency from the microwave domain to the optical domain can be achieved. The hybrid waveguide can be designed as racetrack and spiral microrings to reduce the pump threshold power and enhance the Brillouin optomechanical interaction. Our design scheme is technologically verifiable. This multi-physical interaction can be used in a variety of versatile applications, and the proposed devices will be exceedingly suitable candidates for the integrated silicon photonics.

References

[1] A. G. Krause, M. Winger, T. D. Blasius, Q. Lin, and O. Painter, "A high-resolution microchip optomechanical accelerometer," *Nature. Photon.*, vol. 6, no. 11, pp. 768–772, 2012.

[2] M. Bagheri, M. Poot, L. Fan, F. Marquardt, and H. X. Tang, "Photonic cavity synchronization of nanomechanical oscillators," *Phys. Rev. Lett.*, vol. 111, no. 21, 2013, Art. no. 213902.

[3] M. Zhang, G. S. Wiederhecker, S. Manipatruni, A. Barnard, P. McEuen, and M. Lipson, "Synchronization of micromechanical oscillators using light," *Phys. Rev. Lett.*, vol. 109, no. 23, 2012, Art. no. 233906.

[4] J. Chan *et al.*, "Laser cooling of a nanomechanical oscillator into its quantum ground state," *Nature*, vol. 478, no. 7367, pp. 89–92, 2011.

[5] R. Riedinger *et al.*, "Non-classical correlations between single photons and phonons from a mechanical oscillator," *Nature*, vol. 530, no. 7590, pp. 313–316, 2016.

[6] A. H. Safavi-Naeini, S. Gröblacher, J. T. Hill, J. Chan, M. Aspelmeyer, and O. Painter, "Squeezed light from a silicon micromechanical resonator," *Nature*, vol. 500, no. 7461, pp. 185–189, 2013.

[7] G. S. Agarwal and S. S. Jha, "Multimode phonon cooling via three-wave parametric interactions with optical fields," *Phys. Rev. A*, vol. 88, no. 1, 2013, Art. no. 0 13815.

[8] A. H. Safavi-Naeini, J. Chan, J. T. Hill, T. P. M. Alegre, A. Krause, and O. Painter, "Observation of quantum motion of a nanomechanical resonator," *Phys. Rev. Lett.*, vol. 108, no. 3, 2012, Art. no. 0 33602.

[9] H. Shin *et al.*, "Tailorable stimulated Brillouin scattering in nanoscale silicon waveguides," *Nature Commun.*, vol. 4, no. 1, 2013, Art. no. 1944.

[10] L. Raphaël Van, B. Alexandre, K. Bart, B. Roel, and T. Dries Van, "Net on-chip Brillouin gain based on suspended silicon nanowires," *New J. Phys.*, vol. 17, no. 11, 2015, Art. no. 115005.

[11] R. Van Laer, B. Kuyken, D. Van Thourhout, and R. Baets, "Interaction between light and highly confined hypersound in a silicon photonic nanowire," *Nature Photon.*, vol. 9, no. 3, pp. 199–203, 2015.

[12] E. A. Kittlaus, N. T. Otterstrom, and P. T. Rakich, "On-chip inter-modal Brillouin scattering," *Nature Commun.*, vol. 8, no. 1, 2017, Art. no. 15819.

[13] E. A. Kittlaus, H. Shin, and P. T. Rakich, "Large Brillouin amplification in silicon," *Nature Photon.*, vol. 10, no. 7, pp. 463–467, 2016.

[14] E. A. Kittlaus, N. T. Otterstrom, P. Kharel, S. Gertler, and P. T. Rakich, "Non-reciprocal interband Brillouin modulation," *Nature Photon.*, vol. 12, no. 10, pp. 613–619, 2018.

[15] N. T. Otterstrom, R. O. Behunin, E. A. Kittlaus, Z. Wang, and P. T. Rakich, "A silicon Brillouin laser," *Science*, vol. 360, no. 6393, 2018, Art. no. 1113.

[16] N. T. Otterstrom, E. A. Kittlaus, S. Gertler, R. O. Behunin, A. L. Lentine, and P. T. Rakich, "Resonantly enhanced nonreciprocal silicon Brillouin amplifier," *Optica*, vol. 6, no. 9, pp. 1117–1123, 2019.

[17] S. Gertler, E. A. Kittlaus, N. T. Otterstrom, P. Kharel, and P. T. Rakich, "Microwave filtering using forward Brillouin scattering in photonic-phononic emit-receive devices," *J. Lightw. Technol.*, vol. 38, no. 19, pp. 5248–5261, 2020.

[18] S. Gertler, E. A. Kittlaus, N. T. Otterstrom, and P. T. Rakich, "Tunable microwave-photonic filtering with high out-of-band rejection in silicon," *APL Photon.*, vol. 5, no. 9, 2020, Art. no. 096103.

[19] N. T. Otterstrom *et al.*, "Backscatter-immune injection-locked Brillouin laser in silicon," *Phys. Rev. Appl.*, vol. 14, no. 4, 2020, Art. no. 044042.

[20] A. Ashkin, "Trapping of atoms by resonance radiation pressure," *Phys. Rev. Lett.*, vol. 40, no. 12, pp. 729–732, 1978.

[21] C. Fabre, M. Pinard, S. Bourzeix, A. Heidmann, E. Giacobino, and S. Reynaud, "Quantum-noise reduction using a cavity with a movable mirror," *Phys. Rev. A*, vol. 49, no. 2, pp. 1337–1343, 1994

[22] K. Jacobs, P. Tombesi, M. J. Collett, and D. F. Walls, "Quantum-nondemolition measurement of photon number using radiation pressure," *Phys. Rev. A*, vol. 49, no. 3, pp. 1961–1966, 1994.

[23] Q. Liu, H. Li, and M. Li, "Electromechanical Brillouin scattering in integrated optomechanical waveguides," *Optica*, vol. 6, no. 6, pp. 778–785, 2019.

[24] M. Wu, E. Zeuthen, K. C. Balram, and K. Srinivasan, "Microwave-to-optical transduction using a mechanical supermode for coupling piezoelectric and optomechanical resonators," *Phys. Rev. Appl.*, vol. 13, Jan. 2020, Art. no. 014027.

[25] K. C. Balram, M. I. Davanço, B. R. Ilic, J.-H. Kyhm, J. D. Song, and K. Srinivasan, "Acousto-optic modulation and optoacoustic gating in piezo-optomechanical circuits," *Phys. Rev. Appl.*, vol. 7, Feb. 2017, Art. no. 024008.

[26] H. Ramp *et al.*, "Wavelength transduction from a 3D microwave cavity to telecom using piezoelectric optomechanical crystals," *Appl. Phys. Lett.*, vol. 116, no. 17, 2020, Art. no. 174005.

[27] E. A. Kittlaus, W. M. Jones, P. T. Rakich, N. T. Otterstrom, R. E. Muller, and M. Rais-Zadeh, "Electrically driven acousto-optics and broadband non-reciprocity in silicon photonics," *Nature Photon.*, vol. 15, no. 1, pp. 43–52, 2021.

[28] Z. Cheng, X. Chen, C. Y. Wong, K. Xu, and H. K. Tsang, "Mid-infrared suspended membrane waveguide and ring resonator on silicon-on-insulator," *IEEE Photon. J.*, vol. 4, no. 5, Oct. 2012.

[29] J. S. Penades *et al.*, "Suspended silicon mid-infrared waveguide devices with subwavelength grating metamaterial cladding," *Opt. Exp.*, vol. 24, no. 20, pp. 22908–22916, Oct. 2016.